Autotuning Control System by Variation of Self-Inductance for Dynamic Wireless EV Charging With Small Air Gap

Seog Y. Jeong, *Member, IEEE*, Jun H. Park, *Student Member, IEEE*, Gwang P. Hong, *Student Member, IEEE*, and Chun T. Rim, *Senior Member, IEEE*

***Abstract*—In this paper, an autotuning control system (ACS), which utilizes the variation of self-inductance of a transmitter (Tx) coil caused by a ferrite core of a receiver (Rx), is newly proposed for the dynamic wireless electric vehicle (EV) charging. A Tx module consists of only passive elements that include a Tx coil, a partially compensated capacitor in series with the Tx coil, and a parallel compensation capacitor. All Tx modules share an ac bus line that passes the output filter of an inverter in parallel without any active switches. The current of the coupled Tx coil increases automatically without any manipulations such as controlling the power switches, sensing, or communication when the Rx module is approaching. Not only the system efficiency is increased by the reduction of the conduction losses from the uncoupled Tx modules, but control also becomes simpler because sensors are not required for detecting EVs, and the constant output voltage characteristics can be obtained. Through experiments, it was found that the proposed ACS is suitable for applications such as a tram that runs along an orbit with a small air gap, such as a train. The results showed that the current of a coupled Tx coil increased 11.6 times larger than that of an uncoupled Tx coil, at which time the dc–dc efficiency achieved was 88.4% for an output power of 766 W (10 Ω of load resistance) at the laboratory scale.**

***Index Terms*—Autotuning control system (ACS), dynamic wireless electric vehicle (EV) charging, inductive power transfer system (IPTS), roadway powered electric vehicle (RPEV).**

I. Introduction

IN RECENT years, as concerns about environmental pollution have spread worldwide, the interest in and demand for electric vehicles (EVs) are also increasing and driving an increase in the size of the EV market. However, EVs have the drawback that their charging time is relatively longer and their energy density is low as compared with gasoline vehicles. This results in low mileage per charge when driving. To complement the slow development of batteries and to promote the diffusion

Manuscript received April 6, 2018; revised June 28, 2018; accepted August 12, 2018. Date of publication August 20, 2018; date of current version April 20, 2019. This paper was presented in part at the IEEE PELS Workshop on Emerging Technologies: Wireless Power (WoW), Montréal, PQ, Canada, Jun. 3–7, 2018. Recommended for publication by Associate Editor O. C. Onar. *(Corresponding author: Seog Y. Jeong.)*

The authors are with the Gwangju Institute of Science and Technology (GIST), Gwangju 61005, South Korea (e-mail:

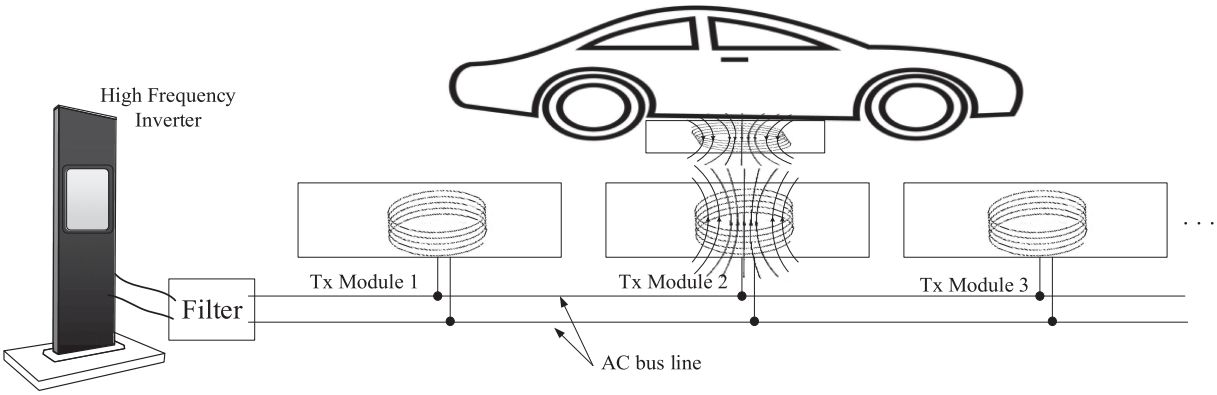

Fig. 1. Overall concept of the proposed ACS.

is more complicated, and requires many sensors and complex control algorithms because many Tx coils are needed to cover a large area.

To reduce the number of inverters, a hybrid type (including multiple inductor-capacitor-capacitor (LCC) compensation for the primary side) of IPTS has also been studied [31]–[34]. These methods may optionally involve active bidirectional switches connected to the output of the inverter to increase the efficiency and reduce the EMF by turning OFF the switches of uncoupled Tx coils. However, it is necessary to sense the presence of the Rx coil, which results in additional sensing circuits for each Tx coil. A research team of San Diego State University proposed the use of an LCC reactive power compensation network to control the Tx current [34]. Instead of connecting bidirectional switches to the output of the inverter to control the Tx current, a reactive power compensation with the LCC compensation circuits is inserted. It still requires an additional sensing circuit for each Tx module because the presence of the Rx is detected by sensing the current of a capacitor inside the reactive power compensation circuit.

Since 2014, research teams, including one at the North Carolina State University, Raleigh, USA, have proposed a reflexive-field containment concept without any active switches or sensors [35]–[38]. The current of the Tx coil is automatically controlled by the reflected capacitive impedance to the primary side by the LCC compensation of the Rx coil. However, the inductance of the Tx coil is generally increased by the presence of the Rx coil regardless of the pad shape, such as circular, DDP, S-type, or even an asymmetric structure of Tx and Rx pads because ferrite cores are used to increase the efficiency and shielding effect on the Rx side. Because of their complementary nature, diminishing current performance could be reduced, if variation in the self-inductance were large, as it would be with small air-gap applications.

In this paper, an autotuning control system (ACS) is proposed that has the advantages of both the centralized and segmented track types. The current of the coupled Tx coil increases automatically without manipulations such as control using the power switches, sensing, and communication when the Rx is approaching. Not only the system efficiency is increased by the reduction of the conduction losses from the uncoupled Tx modules, but control also becomes simpler because sensors are not required for detecting EVs and the constant output voltage (CV) characteristics can be obtained.

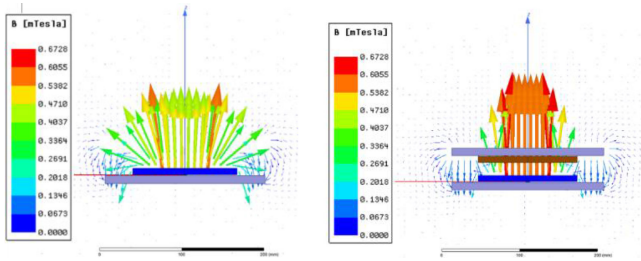

Fig. 2. Magnetic flux distribution for the air gap. (a) Infinity. (b) 110 mm.

II. Proposed ACS for Dynamic Wireless EV Charging

The overall concept of the proposed ACS is shown in Fig. 1. The proposed ACS consists of a high-frequency inverter, bandpass filter, and multiple Tx modules. These Tx modules are implemented only as passive elements consisting of a Tx coil, a partially compensated capacitor in series with the Tx coil, and a parallel compensation capacitor. All the Tx modules share a filter output, called an ac bus line, in parallel without any active switches. To reduce harmonics in the output current of the high-frequency inverter, a bandpass filter is added. The Rx module includes an Rx coil, a compensation circuit, a rectifier, and a regulator for the battery.

A. Key Idea of the Proposed ACS

The key idea of the proposed ACS is to apply the variation of the self-inductance caused by the ferrite cores to the resonant circuit. Fig. 2 (detailed model descriptions are described in the next chapter) shows the magnetic flux distribution with respect to the air-gap variation, where the Tx and Rx coils have a symmetrical-loop coil structure with ferrite cores. The magnetic flux density increases when the Rx module approaches the Tx module because the ferrite core of the Rx module serves as a small reluctance. The magnetic flux density can be increased as much as two times by using a ferrite core [17].

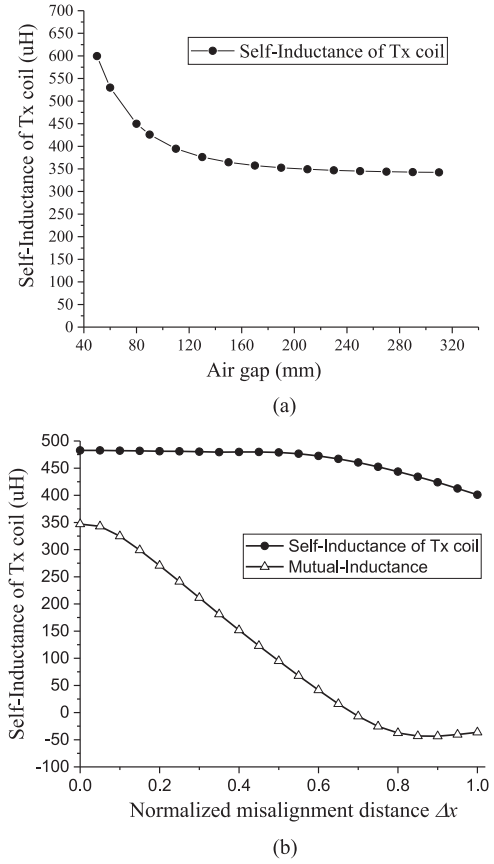

Fig. 3. Self-inductance of the Tx coil with respect to variation in (a) air gap and (b) misalignment along with the moving direction; the condition is based on considering the scale of the simulation model of Fig. 7.

As the magnetic flux density increases, the self-inductance of the Tx coil also increases. Under the simulation conditions of Fig. 2, the self-inductance of the Tx coil is shown with respect to the air-gap variation in Fig. 3(a). It is obvious that the self-inductance of the Tx coil increases as the Rx module (including the ferrite cores) approaches. The self-inductance of the Tx coil and mutual inductance between the Tx and Rx coils are shown with respect to the misalignment along with the moving direction in Fig. 3(b). The self-inductance of the Tx coil also increases as the Rx coil approaches, resulting in a change in the resonance condition of the Tx coil. By way of an example, the movement of the tram is limited; however, the proposed ACS has no particular restriction on the movement of the Rx module.

To explain the basic principle in more detail, the voltage source and series compensation capacitors on both sides are applied as shown in Fig. 4. In this section, all parasitic resistances are neglected to provide a simpler explanation. Fig. 4(a) shows the conventional series–series compensation expressed by a coupled-inductor model. Here, L_p, $L_{\rm lp}$, $L_{\rm mp}$, and ΔL refer to the self-inductance of the Tx coil, leakage inductance of the Tx coil, magnetizing inductance of the Tx coil, and inductance variation of the Tx coil caused by the presence of the Rx coil, respectively. L_s and $L_{\rm ls}$ are self-inductance of the Rx coil and leakage inductance of the Rx coil, respectively. Fig. 4(c) shows the transformer model when the Rx coil is coupled with the Tx coil with load. $L_{\rm lp}$ and $L_{\rm sp}$ are compensated to get the CV

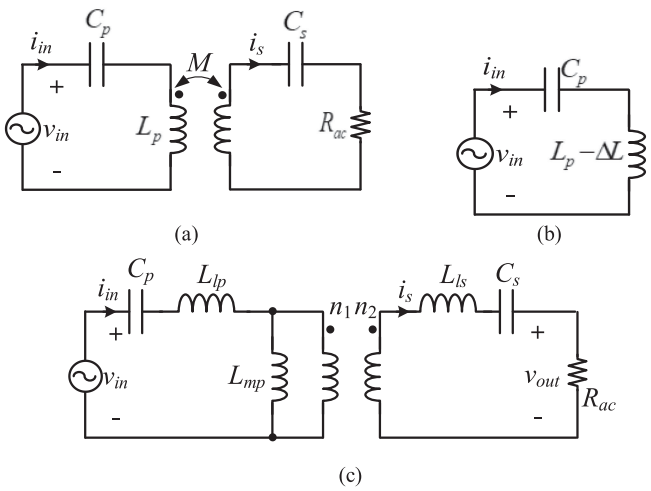

Fig. 4. Typical circuit configuration of IPTS. (a) Coupled inductor model. (b) Equivalent circuit when the Rx module is absent. (c) Transformer model when the Rx module is approaching.

characteristic. The resonant condition is as follows:

$$\omega_r = \frac{1}{\sqrt{L_{lp}C_p}} = \frac{1}{\sqrt{L_{ls}C_s}} \tag{1}$$

where C_p and C_s are the series resonant capacitors for the compensation of $L_{\rm lp}$ and $L_{\rm sp}$, respectively. The switching angular frequency ω_s should be same as the result with (1). In this case, the current of the coupled Tx coil is as follows:

$$I_{\rm in,coupled} = \frac{V_{\rm in}}{Z_{\rm coupled}} = \frac{V_{\rm in}}{j\omega_s L_{\rm mp}||R_{\rm ac}/n^2} \tag{2}$$

where $V_{\rm in}$ is the input voltage source, the turn ratio n is defined as n_2/n_1, and $R_{\rm ac}$ is the effective load of the Rx module. The relation between $R_{\rm ac}$ and the load resistance R_L for a voltage source rectifier is found to be

$$R_{\rm ac} = \frac{8}{\pi^2}R_L. \tag{3}$$

Fig. 4(b) shows the simplified circuit when the Rx module is absent. The current of the uncoupled Tx coil is defined as follows:

$$I_{\rm in,uncoupled} = \frac{V_{\rm in}}{j\omega_s(L_p - \Delta L) + 1/(j\omega_s C_p)} = \frac{V_{\rm in}}{j\omega_s(L_{mp} - \Delta L)}. \tag{4}$$

By dividing (2) by (4), the current ratio of coupled and uncoupled Tx coils α is defined as follows:

$$\alpha \equiv \frac{|I_{\rm in,coupled}|}{|I_{\rm in,uncoupled}|} = \frac{|Z_{\rm uncoupled}|}{|Z_{\rm coupled}|} = \frac{|j\omega_s\,(L_{mp} - \Delta L)|}{|j\omega_s L_{mp}||R_{ac}/n^2|}. \tag{5}$$

It is important for the design that α is larger than 1. If α is large enough, the EMF problem is resolved automatically without a complex and additional control system. The proposed ACS can be implemented if the impedance of the Tx module ($Z_{\rm uncoupled}$ in the condition that the Rx module is uncoupled) is sufficiently large, or if $R_{\rm ac}$ is sufficiently small, compared to the impedance of $L_{\rm mp}$. Specifically, the current of the coupled

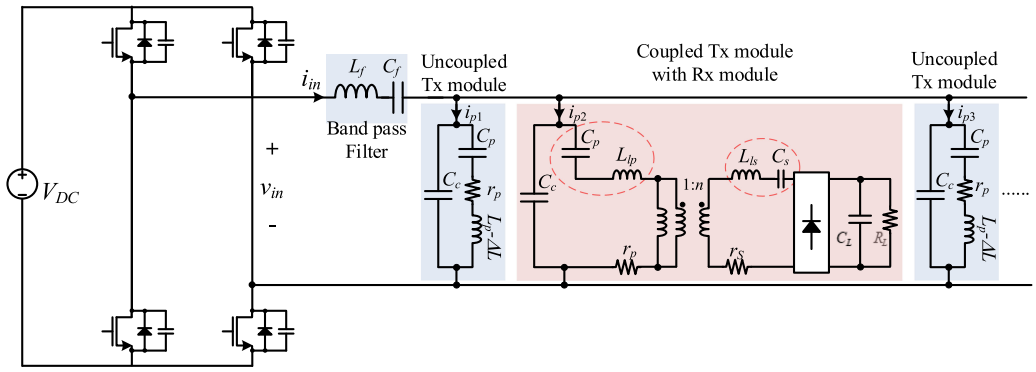

Fig. 5. Equivalent circuit of the proposed ACS.

Tx coils is automatically controlled by the variation of the self-inductance of the Tx coils caused by the influence of the ferrite cores of the Rx module.

B. Static Circuit Analysis of the Proposed ACS

To implement the proposed ACS, multiple Tx modules adding additional capacitors in parallel are considered as shown in Fig. 5. All parasitic resistances are neglected and all Tx coils are assumed to be decoupled for a simpler analysis. If the Tx module consists solely of the Tx coil and C_p, a large reactive current can flow from the inverter output, resulting in malfunction of the inverter. Therefore, an additional compensation capacitor C_c was inserted into the Tx module. There, C_c is placed in parallel to each Tx module to reduce the conduction loss and instability of the ac bus line. The total price of the proposed ACS could decrease in proportion to the number of Tx modules, which is connected to the output of the inverter in parallel, under the same power delivery conditions. When the Rx module is absent, the capacitance C_c for parallel resonance in each module is as follows:

$$\frac{1}{j\omega_s C_c} = -Z_{\text{uncoupled}} = -j\omega_s \left(L_{\text{mp}} - \Delta L\right). \tag{6}$$

The inverter does not ideally provide any current in steady state when the Rx module is absent. As a result, high efficiency can be achieved under a light-load or no-load condition. Meanwhile, the magnetizing current from the inverter only begins to flow when the Rx module is approaching the Tx module.

As the load gradually increases, a large amount of current flows through the coupled Tx coil. The bandpass filter formed by L_f and C_f in series simply serves to reduce the output current harmonics of the high-frequency inverter. Using the bandpass filter under the above-mentioned assumptions, the circuit of Fig. 5 can be simplified further by an approximation of the fundamental component as shown in Fig. 6. Finally, the real power P_o and the reactive power Q_o of the inverter are driven by (2) and (3), respectively, as follows:

$$P_o = \frac{n^2 V_{\text{in}}^2}{R_{\text{ac}}} \tag{7a}$$

$$Q_o = V_{\text{in}}^2 \left(\frac{1}{|j\omega L_{mp}|} - \frac{1}{|Z_{\text{uncoupled}}|}\right). \tag{7b}$$

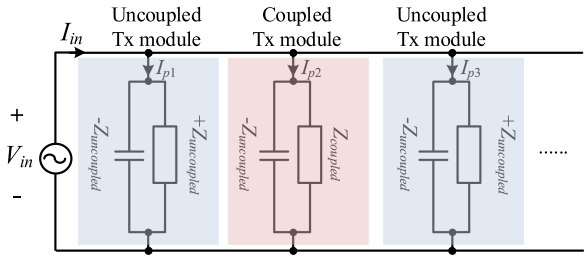

Fig. 6. Simplified circuit of the proposed ACS.

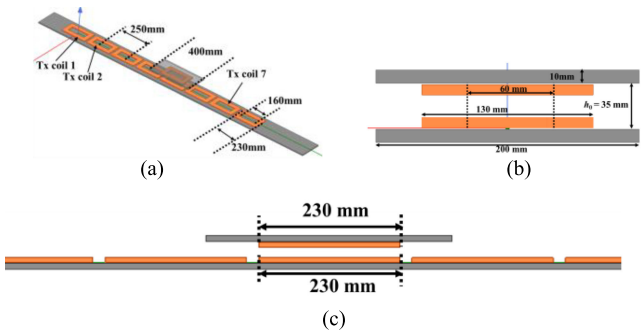

Fig. 7. Overall circuit simulation condition. (a) Bird's eye view of the proposed ACS. (b) Front view. (c) Side view.

Thanks to the topologies of the leakage compensation for both sides, and the power-factor compensation of C_c in each Tx module, CV characteristics, and high efficiency can be achieved at the same time. The system efficiency, the considering parasitic resistance, is found to be

$$\eta_{\text{dc-dc}} = \frac{P_o}{P_{\text{inv}} + \sum P_{Tx\_\text{coil}} + P_{Rx\_\text{coil}} + P_{\text{rec}} + P_o} \approx \frac{\alpha}{\alpha + \omega C_c \{(N_{Tx} - 1 + \alpha^2)\, r_{Tx} + r_{Rx}/n^2\}} \tag{8a}$$

$$\alpha|_{\eta_{\text{dc-dc, max}}} = \sqrt{\frac{\omega C_c \left(N_{Tx} - 1\right) + r_{Rx}/n^2 r_{Tx}}{\omega C_c}} \tag{8b}$$

where N_{Tx} is the number of Tx coil, and r_{Tx} and r_{Rx} are the parasitic resistances of the Tx and Rx coils, respectively. Note that the system efficiency is dominant in loss of the Tx coil

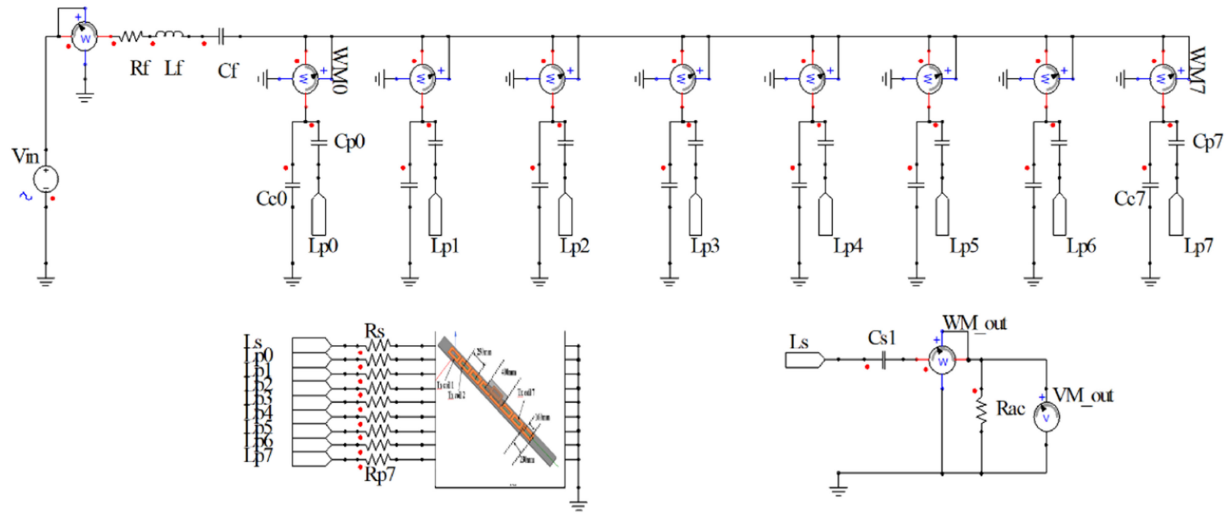

Fig. 8. Multidomain simulator linked with the FEM 3-D of Fig. 7.

for light-load condition, whereas it is dominant in losses of the Rx module for heavy-load condition. The losses could be minimized by increasing $Z_{\text{uncoupled}}$, the operating frequency, or the number of turns of the Tx and Rx coils. The operating frequency should be selected carefully because it affects the system efficiency and stability of the proposed ACS. As the operating frequency increases, the magnetizing current decreases, resulting in minimizing losses because the proposed ACS compensates the leakage inductance in both sides. There is theoretically no restriction in case that all the terminals of the Tx module are connected to the inverter output as common nodes; however, the connection points could be distributed from each other in long track and no longer common nodes, resulting in increased impedance difference by line inductance at every connection point. As a result, the impedance difference of each connection point makes the system unstable with a deviation of the resonance condition in case that the operating frequency is too high.

Moreover, the speed of the Rx module could be limited to the dynamics of the resonant circuit because the proposed ACS uses changing the resonant condition by the ferrite core. Thankfully, it is not comparable to the dynamic response of the resonant circuit that reaches the steady state within a few cycles, since a running speed of a tram operating in the city center is usually less than 60 km/h (even at 600 km/h, the impact on the proposed ACS is negligible because the distance traveled by the tram is less than 2 cm during the 10 cycles of operating frequency of 85 kHz).

III. Simulation Verifications

To identify the operation of the proposed ACS, the three-dimensional (3-D) finite-element analysis Maxwell simulation tool and multidomain simulator Simplorer were used as shown in Figs. 7 and 8, respectively. The mechanical parameters (e.g., size of the ferrite core or coil diameters) were selected in sizes easy to be fabricated at the laboratory scale.

The electrical parameters for the simulation set are described in Table I, where the Tx and Rx coils were all set to the same value. All the magnetic couplings between the Tx and Rx coils

TABLE I
Simulation Key Parameters

Para.	Value	Para.	Value	Para.	Value
L_p & L_s	483 [μH]	C_p & C_s	26.4 [nF]	R_p & R_s	400 [mΩ]
L_{lp}&L_{ls}	133 [μH]	C_c	16.94 [nF]	k_{main} (between Rx and *Coupled Tx*)	0.72
L_{mp}	350 [μH]	C_f	87.65 [nF]	k_{max} (between *Tx coils*)	-0.04
ΔL	143 [μH]	N_1 & N_2	30 [Turns]	k_{max} (between Rx and *uncoupled Tx coil*)	-0.04
L_f	40 [μH]	Operating frequency	85 [kHz]	-	-

were considered and simulated for more accurate results. As shown in Table I, the coupling coefficient k_{main} between the coupled Tx and Rx coils is 0.72 when the Rx coil is perfectly aligned with a singular Tx coil. In this case, the Rx coil is coupled with the Tx coil 1. In the case of a tram-charging application unlike the EV charging applications, the coupling coefficient could easily exceed 0.5 due to the relatively small air gap and large installation area. The rest of the coupling coefficients were smaller than 0.04. Even when the Rx coil is in the middle of two Tx coils, the coupling coefficient between the Tx coils with respect to the position of the Rx coil kept at low values (always less than 0.04) in various positions compared to the main coupling. Thus, the assumption in previous sections about the decoupling of each Tx coil was reasonable.

Using the parameters in Fig. 7 and Table I, the current of the Tx coils with respect to the load condition was simulated and is shown in Fig. 9. As expected, the current gain for the coupled Tx coil was only boosted under different load conditions. Under the condition that R_{ac} is 10 Ω, the current of the coupled Tx coil was boosted about 11 times. The current of the coupled Tx coil was also observed to shift from the lagging to the resistive, as the load became heavy in condition. Meanwhile, the current of the uncoupled Tx coils was always constant, regardless of the load variation. Moreover, despite the parasitic resistance of

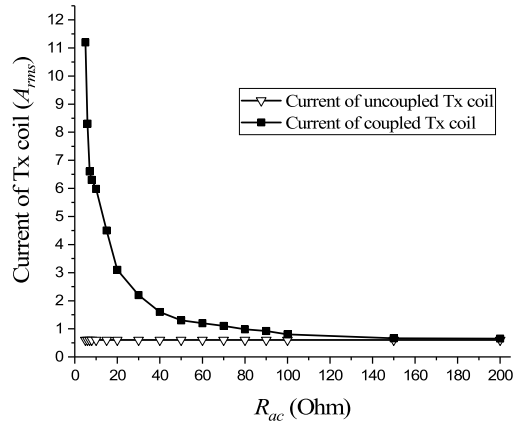

(a)

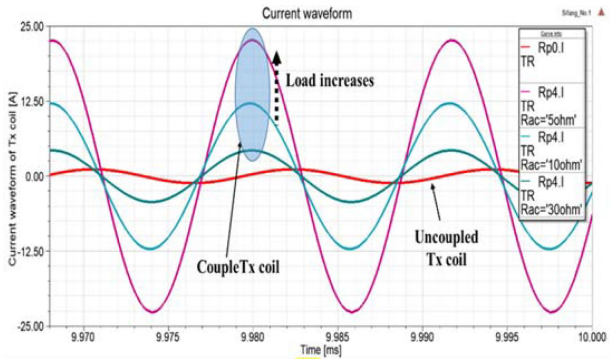

(b)

Fig. 9. Simulation result for the current of each Tx coil. (a) RMS value of the Tx coils. (b) Current waveforms of the Tx coils.

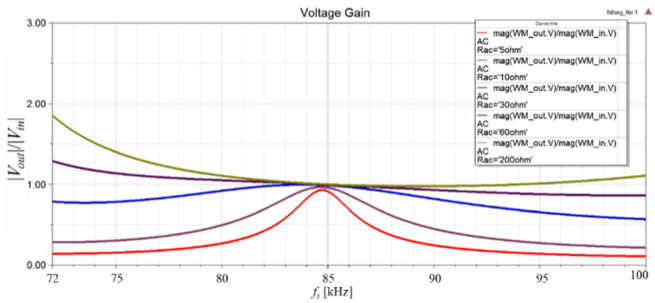

Fig. 10. Simulation results of voltage gain $V_{\text{out}}/V_{\text{in}}$ with respect to the load variation.

400 mΩ in each Tx and Rx coils, the CV characteristic was also achieved (within 5% variation) over a wide range of load conditions (5–200 Ω) as shown in Fig. 10.

To verify the soft-switching condition and reduced input current of the inverter during travel, the frequency response of the input impedance with respect to misalignment of the moving direction is shown in Fig. 11. The Rx coil has moved from the center of a fully coupled Tx coil to the middle of two Tx coils, keeping the load resistance of 5 Ω. When the Rx coil is fully coupled with the Tx coil, the phase of input impedance is 1.42° while maintaining soft switching condition margins. As the Rx coil moves to the middle of the two Tx coils, the phase of input

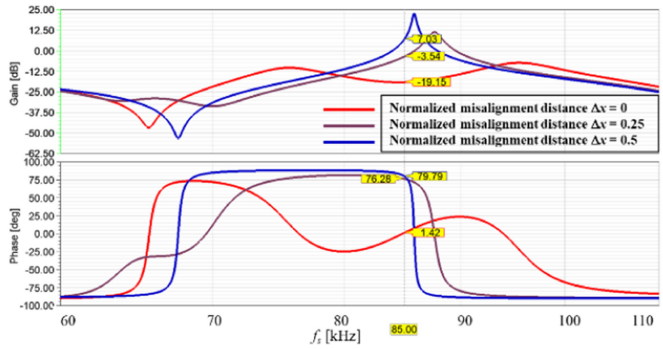

Fig. 11. Simulation results of the frequency response of the input impedance.

impedance converges to 90°, where the gain of input impedance increases to 24 dB, corresponding to 15.8 times. Soft switching is possible over the entire traveling, and the input impedance increases when the power is not transferred to the Rx module, thereby reducing the loss, namely, it is controlled without changing the operating frequency for different positions of the Rx module.

The proposed ACS can also operate with multiple Rx modules because it is possible to achieve the CV characteristic of each Rx module without changing the resonant condition in case that each Tx module is coupled with a singular Rx module. The number of coupled Tx modules (red color) in the circuit as shown in Fig. 6 is increased as multiple in parallel.

IV. Experimental Results

A prototype operating at 85 kHz was fabricated, as shown in Fig. 12, to verify its feasibility. Seven pairs of Tx coils and an Rx coil were fabricated with the same size as in the simulation conditions in the previous section. The end point of each Tx module was connected to the output of the filter in parallel through the ac bus line made of an aluminum bar to eliminate any problem of instability. 100 V_{dc} was applied to the input of the full-bridge inverter because the input of the oscilloscope has only four channels, and all results are shown for only four channels.

The measured current of the coupled Tx coil was 11.6 times larger than the current of the uncoupled Tx coils under the conditions that the Rx module was aligned to the Tx module 3, and that R_L was 10 Ω, as shown in Fig. 13(a), where the output power and efficiency are 766 W and 88.4%, respectively. In the case in which R_L was 6 Ω, the current ratio of the coupled–uncoupled Tx coils α was 18.1, where the output power and efficiency were 1232 W and 81.8%, respectively. The measured maximum efficiency was 96.7% for R_L of 100 Ω.

The power loss analysis of the proposed ACS for a different load condition is shown in Fig. 14 while the load power is maintained at 1 kW. To apply to a real tram model, the input dc voltage should be changed to 750 V, which is often applied to trams in the industry, resulting in an increased power to 56 times. The dominant losses are found to be the resistance of the coupled Tx and Rx coils, which includes a hysteresis loss of the ferrite core, since most of the currents are concentrated

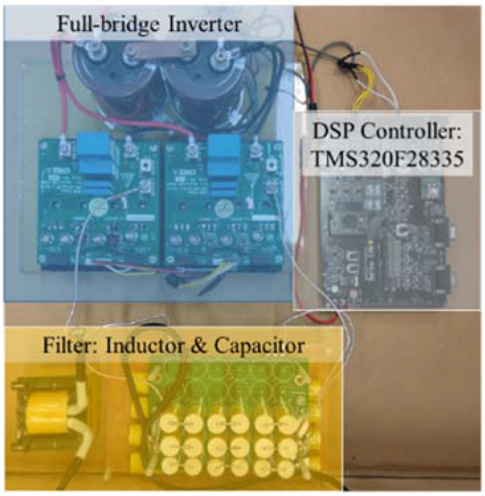

(a)

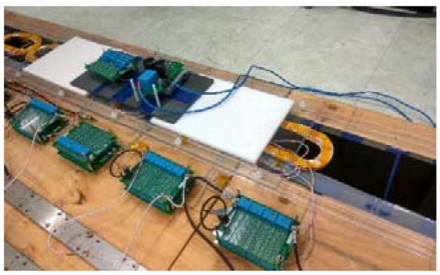

(b)

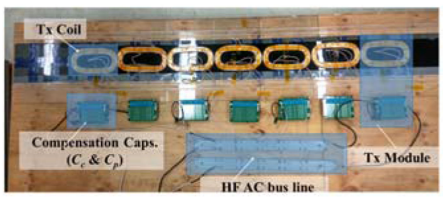

(c)

Fig. 12. Experimental conditions. (a) Inverter and bandpass filter. (b) ACS including the Rx module. (c) Tx modules without the Rx module.

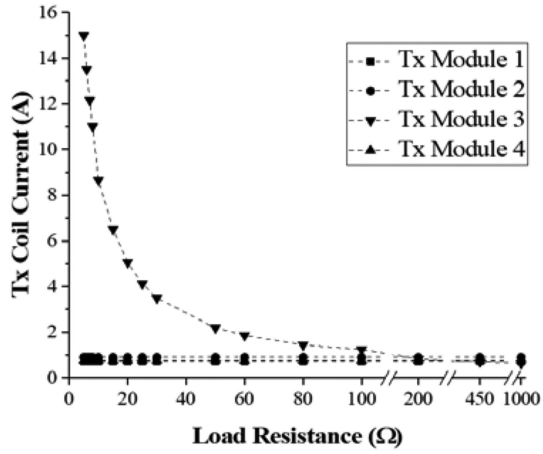

(a)

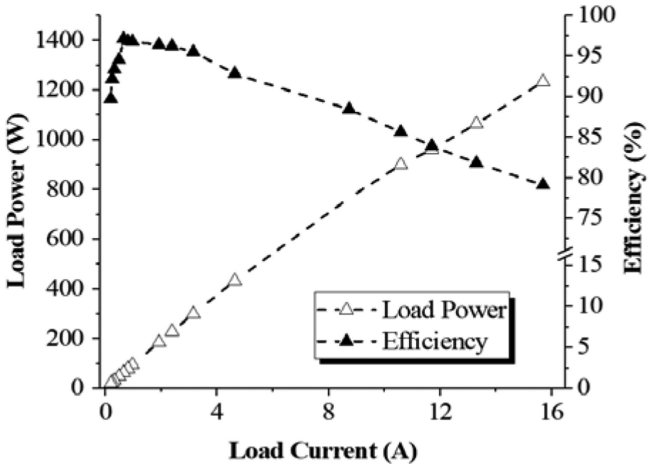

(b)

Fig. 13. Experimental results. (a) RMS value of the Tx coil current. (b) Output power and efficiency.

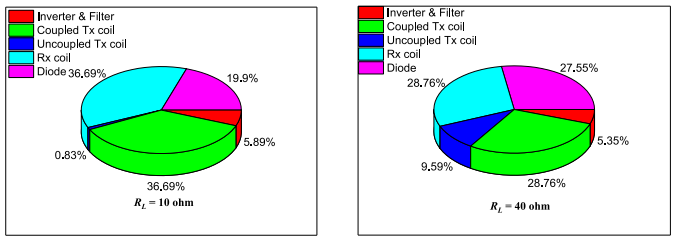

(a) (b)

Fig. 14. Example of the power loss analysis of the proposed ACS when (a) $R_L = 10\,\Omega$, and (b) $R_L = 40\,\Omega$.

at the coupled Tx coil for a higher α condition, as expected. It means that the system efficiency is inversely proportional to the number of Tx coils; however, it is relatively negligible for a higher α condition. Although the conduction losses of the diode consisting of four full-bridge configurations seem to account for more than a quarter of total losses, the system efficiency can be increased by replacing the synchronous rectifier. Depending on the current ratio and efficiency, the number of turns in the Tx and Rx coils can be adjusted to move the maximum efficiency point by decreasing the turn ratio *n*. Therefore, an optimization of coil size should be developed to increase the system efficiency for further works.

According to the International Commission on Non-Ionizing Radiation Protection (ICNIRP) guideline, the leakage magnetic-field density is limited to less than 27 μT at 85 kHz. To check the EMF level, the EMF around the Tx coil of the proposed ACS was measured using ELT-400 made by Narda as shown in Fig. 15. The electric field is not measured since the magnetic field is dominant in the near-field range. The measured point is 350 mm from the center of the Tx coil while maintaining the medium of the air gap, where the measured point was calculated by the actual width of the tram of 2.5 m and the separation distance for measurement of 200 mm, according to the ICNIRP guideline.

Fig. 16 shows the EMF level generated from the proposed ACS. The experiments were performed at a load power of 1 kW; however, the magnetic field, which is proportional to the input voltage, was multiplied by 7.5 times considering the load power of 40 kW. It was as low as 9.84 and 8.25 μT at a distance of

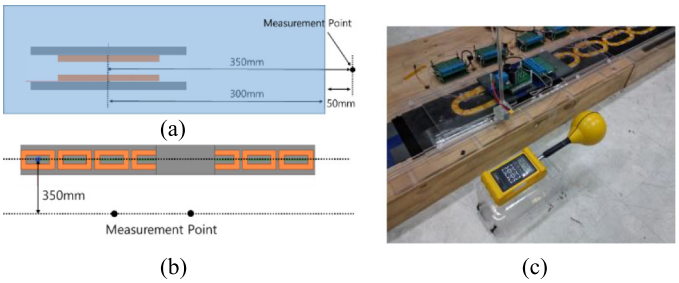

Fig. 15. EMF measurement method. (a) Front view. (b) Top view. (c) Experimental setup.

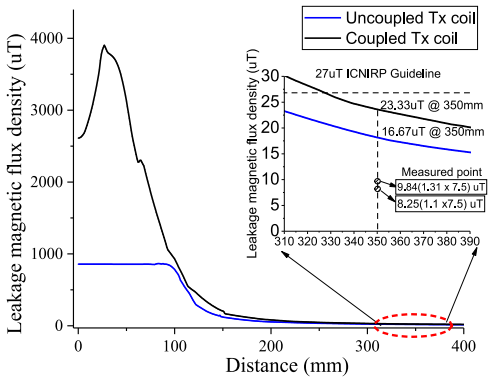

Fig. 16. EMF level for a pedestrian side; measurement (point of 350 mm); simulations (continuous line).

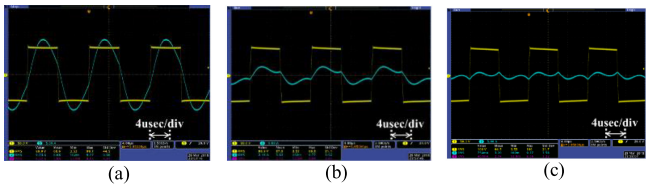

Fig. 17. Voltage and current waveforms of the inverter for a perfectly aligned condition. Ch. 1: inverter output voltage (50 V/div) and Ch. 2: inverter output current (5 A/div), when (a) $R_L = 10\,\Omega$, (b) $R_L = 50\,\Omega$, and (c) $R_L = \infty$.

350 mm for the coupled and uncoupled Tx coils, respectively. This is merely a kind of an error caused by a relatively large magnetic probe and still meets the ICNIRP guideline.

Fig. 17 shows the output voltage and current waveforms of the inverter when the Rx module is aligned to the Tx module 3. The waveforms show that the inverter current decreases to almost zero under no-load condition. Zero voltage switching can also be achieved using harmonics of the inverter current.

Figs. 18 and 19 show the transient mode for the current of each Tx coil. The current of the coupled Tx coil (see Ch. 3 of the oscilloscope in Fig. 13) increases depending on the load conditions without affecting the uncoupled Tx coils. Even if the load condition changed rapidly, the current of the uncoupled Tx coils was not affected. The current of each Tx coil is shown in Fig. 19 as the Rx module moves past them along the track. The current of each Tx coil increases only when the Rx module approaches and keeps constant when the Rx module is absent.

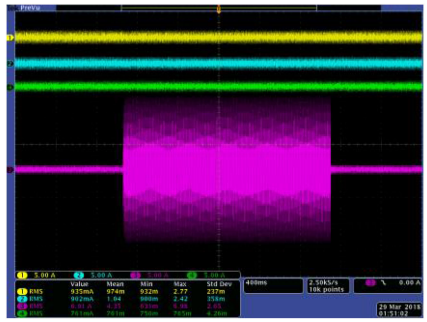

Fig. 18. Tx coil current waveforms: Ch. 1, Ch. 2, and Ch. 4 (uncoupled Tx coils), and Ch. 3 (coupled Tx coil) when the Rx module is aligned.

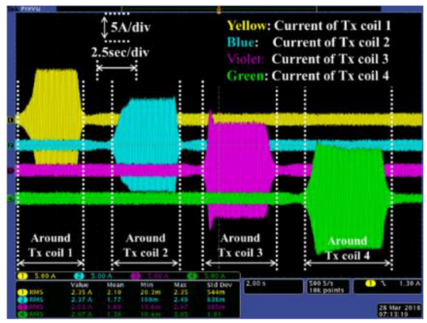

Fig. 19. Tx coil waveforms when the Rx moves past them along the track.

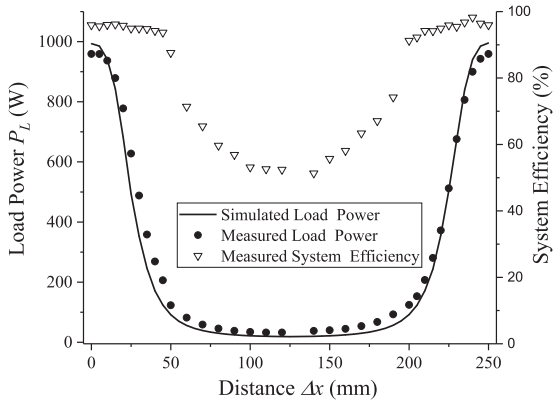

Fig. 20. Measured load power and system efficiency of the proposed ACS with respect to the position of Rx module.

To verify the autotuning capability of the proposed ACS over the moving direction, the load power and system efficiency (dc–dc) was measured by moving the Rx module with respect to the Tx module as shown in Fig. 20. The system is designed to be 1 kW of load power when the Rx module is well aligned with the Tx module. As expected from Fig. 3, the maximum power can be transferred when the Tx and Rx coils are fully coupled similar to the conventional dynamic charging. The load power rapidly drops as the Rx module moves to the middle of the two Tx modules due to the deviation of the resonance condition by the reduction of the magnetizing inductance. The efficiency of the proposed system is relatively kept high by the reduction of the current in the Tx coil. The proposed idea is verified for a small air-gap application, such as a tram, which can run along the fixed track.

V. Conclusion

A new IPTS topology, the ACS, was proposed that utilizes the variation of self-inductance of Tx coils caused by ferrite cores in the Rx module. The proposed ACS has the advantages of reducing the EMF, being cost effective, and having high efficiency because no additional sensors and controllers are required for detecting the EVs. Through experiments, it was found that the proposed ACS is suitable for applications such as a tram that runs along an orbit with a small air gap. The results showed that the current of a coupled Tx coil increased 11.6 times larger than that of an uncoupled Tx coil, at which time the dc–dc efficiency achieved was 88.4% for an output power of 766 W (10 Ω of load resistance) at the laboratory scale.

References

[1] J. Huh, S. W. Lee, W. Y. Lee, G. H. Cho, and C. T. Rim, "Narrow-width inductive power transfer system for online electrical vehicles," *IEEE Trans. Power Electron.*, vol. 26, no. 12, pp. 3666–3679, Dec. 2011.

[2] S. Lee, B. Choi, and C. T. Rim, "Dynamics characterization of the inductive power transfer system for online electric vehicles by Laplace phasor transform," *IEEE Trans. Power Electron.*, vol. 28, no. 12, pp. 5902–5909, Dec. 2013.

[3] S. Choi, J. Huh, S. Lee, and C. T. Rim, "New cross-segmented power supply rails for roadway powered electric vehicles," *IEEE Trans. Power Electron.*, vol. 28, no. 12, pp. 5832–5841, Dec. 2013.

[4] S. Y. Choi, S. Y. Jeong, E. S. Lee, B. W. Gu, S. W. Lee, and C. T. Rim, "Generalized models on self-decoupled dual pick-up coils for a large lateral tolerance," *IEEE Trans. Power Electron.*, vol. 30, no. 11, pp. 6434–6445, Nov. 2015.

[5] S. Y. Choi, B. W. Gu, S. Y. Jeong, G. C. Lim, and C. T. Rim, "Ultra slim s-type power supply rails for roadway powered electric vehicles," *IEEE Trans. Power Electron.*, vol. 30, no. 11, pp. 6456–6468, Nov. 2015.

[6] C. Park, S. Lee, S. Y. Jeong, G. H. Cho, and C. T. Rim, "Uniform power I-type inductive power transfer system with DQ-power supply rails for on-line electric vehicles," *IEEE Trans. Power Electron.*, vol. 30, no. 11, pp. 6446–6455, Nov. 2015.

[7] S. Y. Choi, B. W. Gu, S. Y. Jeong, and C. T. Rim, "Advances in wireless power transfer systems for roadway powered electric vehicles," *IEEE J. Emerg. Sel. Topics Power Electron*., vol. 3, no. 1, pp. 18–36, Mar. 2015.

[8] C. Mi, G. Buja, S. Y. Choi, and C. T. Rim, "Modern advances in wireless power transfer systems for roadway powered electric vehicles," *IEEE Trans. Ind. Electron.*, vol. 63, no. 10, pp. 6533–6545, Oct. 2016.

[9] W. Y. Lee *et al.*, "Finite-width magnetic mirror models of mono and dual coils for wireless electric vehicles," *IEEE Trans. Power Electron.*, vol. 28, no. 3, pp. 1413–1428, Mar. 2013.

[10] S. Y. Choi, B. W. Gu, S. W. Lee, W. Y. Lee, J. Huh, and C. T. Rim, "Generalized active EMF cancel methods for wireless electric vehicles," *IEEE Trans. Power Electron.*, vol. 29, no. 11, pp. 5770–5783, Nov. 2014.

[11] V. X. Thai, S. Y. Choi, B. H. Choi, J. H. Kim, and C. T. Rim, "Coreless power supply rails compatible with both stationary and dynamic charging of electric vehicles," in *Proc. IEEE 2nd Int. Future Energy Electron. Conf.*, 2015, pp. 1–5.

[12] S. Lee *et al.*, "Active EMF cancellation method for I-type pick-up of on-line electric vehicles (OLEV)," in *Proc. 26th Annu. IEEE Appl. Power Electron. Conf. Expo.*, 2011, pp. 1980–1983.

[13] J. Huh, W. Y. Lee, G. H. Cho, B. H. Lee, and C. T. Rim, "Characterization of novel inductive power transfer systems for on-line electric vehicles (OLEV)," in *Proc. 26th Annu. IEEE Appl. Power Electron. Conf. Expo.*, 2011, pp. 1975–1979.

[14] J. H. Kim, B. S. Lee, J. H. Lee, and J. H. Baek, "Development of 1 MW inductive power transfer system for a high speed train," *IEEE Trans. Ind. Electron.*, vol. 62, no. 10, pp. 6242–6250, Oct. 2015.

[15] S. Y. Jeong, J. H. Par, P. H. Gwang, and C. T. Rim, "Auto tuning topology using self-inductance variation for dynamic wireless charging," in *Proc. IEEE WoW 2018*, pp. 1–5.

[16] W. Zhang, S.-C. Wong, C. K. Tse, and Q. Chen, "An optimized track length in roadway inductive power transfer systems," *IEEE J. Emerg. Sel. Topics Power Electron.*, vol. 2, no. 3, pp. 598–608, Sep. 2014.

[17] M. L. G. Kissin, H. Hao, and G. A. Covic, "A practical multiphase IPT system for AGV and roadway applications," in *Proc. IEEE Energy Convers. Congr. Expo.*, 2010, pp. 1844–1850.

[18] S. Zhou and C. C. Mi, "Multi-paralleled LCC reactive power compensation networks and their tuning method for electric vehicle dynamic wireless charging," *IEEE Trans. Ind. Electron.*, vol. 63, no. 10, pp. 6546–6556, Oct. 2016.

[19] G. A. Covic, L. G. Kissin, D. Kacprzak, N. Clausen, and H. Hao, "A bipolar primary pad topology for EV stationary charging and highway power by inductive coupling," in *Proc. IEEE Energy Convers. Congr. Expo.*, 2011, pp. 1832–1838.

[20] G. A. Covic and J. T. Boys, "Modern trends in inductive power transfer for transportation applications," *IEEE J. Emerg. Sel. Topics Power Electron.*, vol. 1, no. 1, pp. 28–41, Mar. 2013.

[21] O. C. Onar, J. M. Miller, M. Chinthavali, and P. T. Jones, "ORNL developments in stationary and dynamic wireless charging applications," presented at the *IEEE Appl. Power Electron. Conf. Expo.*, 1201 Houston St, Fort Worth, USA: fort worth convention center, Mar. 19, 2014.

[22] S. E. Schladover, "Systems engineering of the roadway powered electric vehicle technology," presented at the 9th Int. Elect. Veh. Symp., Toronto, ON, Canada, Nov. 13–16, 1988.

[23] J. G. Bolger, "Urban electric transportation systems: The role of magnetic power transfer," in *Proc. WESCON*, 1994, pp. 41–45.

[24] M. Hanazawa, N. Sakai, and T. Ohira, "SUPRA: Supply underground power to running automobiles: Electric vehicle on electrified roadway exploiting RF displacement current through a pair of spinning tires," in *Proc. IEEE Int. Elect. Veh. Conf.*, Greenville, SC, USA, 2012, pp. 1–4.

[25] J. Shin *et al.*, "Design and implementation of shaped magnetic-resonance based wireless power transfer system for roadway-powered moving electric vehicles," *IEEE Trans. Ind. Electron.*, vol. 61, no. 3, pp. 1179–1192, Mar. 2014.

[26] G. A. Covic, J. T. Boys, M. Kissin, and H. Lu, "A three-phase inductive power transfer system for roadway power vehicles," *IEEE Trans. Ind. Electron.*, vol. 54, no. 6, pp. 3370–3378, Dec. 2007.

[27] G. A. J. Elliott, G. A. Covic, D. Kacprzak, and J. T. Boys, "A new concept: Asymmetrical pick-ups for inductively coupled power transfer monorail systems," *IEEE Trans. Magn.*, vol. 42, no. 10, pp. 3389–3391, Oct. 2006.

[28] L. Chen, G. R. Nagendra, J. T. Boys, and G. A. Covic, "Double-coupled systems for IPT roadway applications," *IEEE J. Emerg. Sel. Topics Power Electron.*, vol. 3, no. 1, pp. 37–49, Mar. 2015.

[29] G. R. Nagendra, G. A. Covic, and J. T. Boys, "Sizing of inductive power pads for dynamic charging of EVs on IPT highways," *IEEE Trans. Transp. Electrific.*, vol. 3, no. 2, pp. 405–417, Jun. 2017.

[30] A. Zaheer and G. A. Covic, "A comparative study of various magnetic design topologies for a semi-dynamic EV charging application," in *IEEE 2nd Annu. Southern Power Electron. Conf.*, Dec. 2016, pp. 1–6.

[31] Q. Zhu, L. Wang, Y. Guo, C. Liao, and F. Li, "Applying LCC compensation network to dynamic wireless EV charging system," *IEEE Trans. Ind. Electron.*, vol. 63, no. 10, pp. 6557–6567, Oct. 2016.

[32] Y. Guo, L. Wang, Q. Zhu, C. Liao, and F. Li, "Switch-on modeling and analysis of dynamic wireless charging system used for electric vehicles," *IEEE Trans. Ind. Electron.*, vol. 63, no. 10, pp. 6568–6579, Oct. 2016.

[33] Y. Wang *et al.*, "A dynamic wireless power transfer system with parallel transmitters," in *Proc. IEEE Transp. Electrific. Conf. Expo, Asia-Pacific*, Aug. 2017, pp. 1–6.

[34] F. Lu, H. Zhang, H. Hofmann, and C. C. Mi, "A dynamic charging system with reduced dynamic wireless EV charging system," *IEEE Trans. Ind. Electron.*, vol. 63, no. 10, pp. 6580–6590, Oct. 2016.

[35] K. B. Lee, Z. Pantic, and S. M. Lukic, "Reflexive field containment in dynamic inductive power transfer systems," *IEEE Trans. Power Electron.*, vol. 29, no. 9, pp. 4592–4602, Sep. 2014.

[36] K. Hemant, B. Manuele, and B. Giuseppe, "Reflexive properties for different pick-up circuit topologies in a distributed IPT track," in *Proc. IEEE 13th Int. Conf. Ind. Inform.*, 2015, pp. 69–75.

[37] H. K. Dashora, S. Giacomuzzi, M. Bertoluzzo, and G. Buja, "Performance analysis of segmentation-reflexive DWC systems with capacitor-based compensation networks," in *Proc. 42nd Annu. Conf. IEEE Ind. Electron. Soc.*, 2016, pp. 4535–4540.

[38] D. Alireza and S. Lukic, "Saturable inductors for superior reflexive field containment in inductive power transfer systems," in *Proc. IEEE Appl. Power Electron. Conf. Expo.*, 2018, pp. 3183–3188.

[39] F. Lu, H. Zhang, H. Hofmann, Y. Mei, and C. Mi, "A dynamic capacitive power transfer system with reduced power pulsation," in *Proc. IEEE PELS Workshop Emerg. Technol.: Wireless Power Transfer*, 2016, pp. 60–64.
[40] S. Li, Z. Liu, H. Zhao, L. Zhu, C. Shuai, and Z. Chen, "Wireless power transfer by electric field resonance and its application in dynamic charging," *IEEE Trans. Ind. Electron.*, vol. 63, no. 10, pp. 6602–6612, Oct. 2016.
[41] C. W. V. Neste, A. Phani, R. Hull, J. E. Hawk, and T. Thundat, "Quasi-wireless capacitive energy transfer for the dynamic charging of personal mobility vehicles," in *Proc. IEEE PELS Workshop Emerg. Technol.: Wireless Power Transfer*, 2016, pp. 196–199.
[42] S. Y. Jeong, H. G. Kwak, G. C. Jang, and C. T. Rim, "Living object detection system based on comb pattern capacitive sensor for wireless EV chargers," *IEEE 2nd Annu. Southern Power Electron. Conf.*, 2016, pp. 1–6.
[43] V. X. Thai, J. H. Park, S. Y. Jeong, and C. T. Rim, "Multiple comb pattern based living object detection with enhanced resolution design for wireless electric vehicle chargers," in *IEEE PCIM Europe; Int. Exhib. Conf. Power Electron., Intell. Motion, Renewable Energy Energy Manage.*, pp. 1–7, 2018.
[44] S. Y. Jeong, V. X. Thai, J. H. Park, and C. T. Rim, "Self-inductance based metal object detection with mistuned resonant circuits and nullifying induced voltage for wireless EV chargers," *IEEE Trans. Power Electron.*, Mar. 2018, doi: 10.1109/TPEL.2018.2813437.
[45] S. Y. Jeong, H. G. Kwak, G. C. Jang, S. Y. Choi, and C. T. Rim, "Dual-purpose nonoverlapping coil sets as metal object and vehicle position detections for wireless stationary EV chargers," *IEEE Trans. Power Electron.*, vol. 33, no. 9, pp. 7387–7397, Oct. 2017.
[46] National Cancer Institute, May 27, 2016. [Online]. Available:https://www.cancer.gov/about-cancer/causes-prevention/risk/radiation/electromagnetic-fields-fact-sheet
[47] American Medical Association, Aug. 5, 1992. [Online]. Available:https://www.ncbi.nlm.nih.gov/pubmed/1629994
[48] Enviromental Health Trust, Apr. 1, 2017. [Online]. Available:https://ehtrust.org/athens-medical-association-recommends-reducing-electromagnetic-wireless-radiation-protect-public-health/

Seog Y. Jeong (S'14–M'18) received the B.S. degree in electrical engineering from Kyungpook National University, Daegu, South Korea, in 2012, and the M.S and Ph.D. degrees in nuclear quantum engineering from the Korea Advanced Institute of Science and Technology (KAIST), Daejeon, South Korea, in 2015 and 2018, respectively.

He is currently a Postdoctoral Researcher at Gwangju Institute of Science and Technology (GIST), Gwangju, South Korea. His research interests include roadway-powered electric vehicle (RPEV) and wireless power transfers (WPT).

Jun H. Park (S'17) received the B.S. degree in electronic engineering from Hanyang University, Seoul, South Korea, in 2017. He is currently working toward the M.S. degree at Gwangju Institute of Science and Technology (GIST), Gwangju, South Korea.

His research interests include roadway-powered electric vehicle (RPEV) and wireless power transfer (WPT).

Gwang P. Hong (S'18) received the B.S. degree in electronic engineering from Gwangju Institute of Science and Technology (GSIT), Gwangju, South Korea, in 2018. He is currently working toward the M.S. degree at Gwangju Institute of Science and Technology.

His research interests include roadway-powered electric vehicle (RPEV), wireless power transfer (WPT), and power systems.

Chun T. Rim (M'90–SM'11) received the B.S. degree with Honors in electrical engineering (EE) from the Kumoh National Institute of Technology (KIT), Gumi, South Korea, in 1985, and the M.S. and Ph.D. degrees in EE from the Korea Advanced Institute of Science and Technology (KAIST), Daejeon, South Korea, in 1987 and 1990, respectively.

During 2007–2016, he was an Associate Professor at KAIST, and currently, he is a Full Professor at the Gwangju Institute of Science and Technology (GIST), Gwangju, South Korea. He has authored or coauthored 160 technical papers and 14 books, and holds 150 patents (awarded and pending).

Dr. Rim won numerous awards, including the Best Paper Award of IEEE TRANSACTIONS ON POWER ELECTRONICS in 2015 and IEEE JOURNAL OF EMERGING AND SELECTED TOPICS IN POWER ELECTRONICS in 2016, both in wireless power transfer (WPT). He is now an Associate Editor of IEEE TRANSACTIONS ON POWER ELECTRONICS and IEEE JOURNAL OF EMERGING AND SELECTED TOPICS IN POWER ELECTRONICS, a Guest Editor of the special issue on WPT of the IEEE TRANSACTIONS ON POWER ELECTRONICS, IEEE TRANSACTIONS ON INDUSTRIAL ELECTRONICS, and IEEE JOURNAL OF EMERGING AND SELECTED TOPICS IN POWER ELECTRONICS, and the General Chair of the 2015 and 2016 IEEE Workshop on Wireless power (WoW).